Journal of Geophysical Research Oceans
August 2008, Volume 113, C08034, NIL_1-NIL_12
http://dx.doi.org/10.1029/2007JC004712

An edited version of this paper was published by AGU.

Generation of tropical instability waves in the Atlantic Ocean

K. von Schuckmann[1, *], P. Brandt[2], C. Eden[2]

[1] IFREMER Brest, Plouzané, France
[2] Leibniz-Institut für Meereswissenschaften, Kiel, Germany

*: Corresponding author : K. von Schuckmann, email address : Karina.Von.Schuckmann@ifremer.fr

Abstract:

The spatial and temporal distributions of tropical instability waves (TIWs) in the Atlantic Ocean are investigated using a combination of current observations with moored instruments deployed at the equator at 23°W and a realistic eddy-resolving (1/12°) general circulation model of the Atlantic Ocean. The meridional and vertical shears of the zonal current system contribute to the eddy production rates and thus to the generation of TIWs in the central tropical Atlantic Ocean. In the Southern Hemisphere, TIWs are forced only by baroclinic instability associated with the vertical shear of the central part of the South Equatorial Current (SEC). In the Northern Hemisphere, baroclinic instability due to the vertical shear of the northern SEC (nSEC) as well as barotropic instabilities due to horizontal shears of the Equatorial Undercurrent (EUC)/nSEC and nSEC/North Equatorial Countercurrent (NECC) contribute to the generation of the TIWs. Since seasonal changes of the instability production rates related to the EUC/nSEC are comparable low while the rates related to the nSEC/NECC are high, we suggest that the seasonality of the NECC dominates the seasonal modulation of the TIWs.

Keywords: tropical instability waves; tropical Atlantic; barotropic and baroclinic instability.

1. Introduction

With the growing data coverage of the global ocean during the last two decades - especially in the near surface layer - it became evident that intraseasonal variability plays a fundamental role in maintaining the heat and freshwater balance by inducing horizontal and vertical fluxes of heat and salt. One of this high frequency variability pattern is referred to as the Tropical Instability Waves (TIWs). Since the early 80th, these waves are known to be a common large scale propagating feature of tropical ocean variability. With their typical periods of 20-40 days and their distinct horizontal signature in the tropical sea surface temperature (SST) fronts they exhibit a characteristic pattern of ocean variability.

The TIWs are believed to be generated by the shear of the tropical zonal current system. They are predominantly excited after the southeast trade winds intensify in boreal spring when the zonal currents in the equatorial band accelerate and the equatorial upwelling intensifies. The TIWs act then in turn to reduce the enhanced shears of the mean zonal currents. Although TIWs are shown to be important for the near surface heat budget of the tropical oceans [e.g. *Weisberg and Weingartner*, 1988; *Grodsky et al.*, 2005; *Peter et al.*, 2006], the detailed generating mechanisms of the TIWs are still under debate, in particular for the tropical Atlantic. On the one hand, TIWs are believed here to be generated predominantly by the meridional shear of the zonal ocean currents, more precisely the shear between the nSEC and the NECC [e.g. *Kelly et al.*, 1995] or the shear between nSEC and the EUC [*Jochum et al.*, 2004]. Barotropic instability than prevails, i.e. instability due to lateral shear of the mean current, and effects of baroclinic

instabilities, i.e. instability related to the vertical shear of the mean current, appear to be negligible [e.g. *Weisberg and Weingartner*, 1988; *Philander et al.*, 1986; *Kelly et al.*, 1995]. On the other hand, *McCreary and Yu* [1992], for example, showed in a numerical simulation that mainly baroclinic instability accounts for the generation of TIWs. *Grodsky et al.* [2005] suggested by analyzing observational data from the equatorial mooring at 23°W that the TIWs are maintained by barotropic and baroclinic conversions and that both instability processes are of comparable size.

Observational and numerical studies have shown that the signature of TIWs are strongest in the northern hemisphere, while TIWs in the southern hemisphere were present but substantially weaker. In the Pacific Ocean, *Lyman et al.* [2007] have shown that different types of TIWs exist, e.g. Yanai waves at a period of about 17 days characterized by fluctuations in meridional velocity at the equator and in subsurface temperature at 2°N and 2°S and unstable Rossby waves at a period of about 33 days characterized by subsurface temperature at 5°N. Because of these differences they argue that the velocity variability on the equator is not directly linked to the TIW signal at 5°N. In the Atlantic Ocean, *Bunge et al.* [2007] have shown that the spatial structure of TIWs is not confined to the equatorial band, suggesting the existence of different types of TIWs. They could not find any clear relation between the northern and southern TIW signatures, indicating that TIWs north and south of the equator do not have the same generating mechanisms. *Han et al.* [2007] have shown that sea level fluctuations associated with TIWs are strong away from the equator, i.e. at 2°-5°N and 2°-5°S,

west of 10°W. In general, these investigations suggest the existence of distinct TIWs depending on the region.

The purpose of the present study is to provide better insight into the spatial structure of the TIWs in the tropical Atlantic Ocean, in particular their (different) generating mechanisms and seasonal modulation using a combination of observational data and a realistic high-resolution (1/12°) general circulation model. The present paper is organized as follows: In section 2, the measurements and model simulations are described. In section 3 the spatial distribution of intraseasonal variability is presented and the model simulations are compared with observations. In section 4, the oscillating patterns at different locations in the tropical Atlantic are investigated. Section 5 describes the eddy kinetic energy (EKE) generating processes for the tropical basin and the last section summarizes and discusses the results.

2. Data and model simulations

2.1. Equatorial moored array observations at 23°W

The current meter mooring at 23°W was deployed several times, supported by different projects. The first deployment period was December-13-2001 to December-21-2002. This mooring was equipped with an upward looking 300-kHz Workhorse ADCP with 4m vertical resolution providing profiles of the horizontal velocity between 130 and 12 m [*Grodsky et al.*, 2005; *Bunge et al.*, 2007]. During the second and third deployment period from February 12, 2004 to May 29, 2005 and from May 29, 2005 to June 19, 2006, the mooring was equipped with two ADCPs, again with an upward-looking 300-kHz Workhorse ADCP, and additionally with a downward-looking 75-kHz Longranger

ADCP with 16m vertical resolution [*Brandt et al.*, 2006, 2007]. The upward-looking Workhorse ADCPs were deployed slightly shallower compared to the first deployment period providing velocity profiles between 100 and 10 m and 80 and 10 m, respectively. The downward-looking Longranger ADCPs below had a measurement range of about 600m. For the second and third deployment period, ADCP data of both instruments have been combined to a continuous data set. The combined data sets have variable depth limits due to mooring motions and in each case have a gap of about 30m arising from the separation of the two ADCP transducers plus their individual blanking distance. These gaps were filled by a Lagrangian interpolation algorithm. Finally the data (5m resolution, 1h intervals) are detided by applying a 40h-low pass filter and by subsequent subsampling to 12h resolution. The measurements of the upward-looking ADCP during the second mooring period are omitted in this investigation as the data seem to be corrupted by a formerly unrecognized instrument failure.

2.2. Model simulation

The eddy-resolving model of the North Atlantic Ocean which we discuss in this study is part of the FLAME-hierarchy (Family of Linked Atlantic Ocean Model Experiments), has horizontal resolution of $1/12^o \cos\phi \times 1/12^o$ (where ϕ denotes the latitude) ranging from about 10 km at the equator to about 5 km in high latitudes. The model domain extends from 20^oS to 70^oN with open boundaries [*Stevens*, 1990] at the northern and southern boundaries and with a restoring zone in the eastern Mediterranean Sea. There are 45 vertical geopotential levels with grid size increasing with depth, ranging from $10\,m$ at the surface to $250\,m$ near the maximal depth of $5500\,m$. The model is based

on a rewritten version[1] of MOM2 [*Pacanowski*, 1995] and is identical to the one used in e.g. *Eden et al.* [2007] where more details about the model configuration can be found. All model results shown here are taken after the 10 year spinup phase.

We will discuss below two experiments with the model. The first is a simple continuation of the spinup for 6 years (experiment CLIM) with the same climatological forcing [*Barnier et al.*, 1995] as in the spinup. This forcing is given by climatological monthly mean wind stress and a Haney-type [*Haney*, 1971] condition for the heat flux for which the net heat flux, apparent atmospheric temperature and damping time scale are also given by monthly means. In the second experiment (DAILY) we have replaced the climatological forcing with daily wind-stress and heat flux forcing from 2001 to 2005 taken from the analysis of the ECMWF T511 numerical weather prediction model with rather high horizontal resolution of approx. 40 $km \times 40$ km. A four-dimensional variational data assimilation scheme was used for producing the ECMWF analysis [*Rabier et al.*, 2000; *Mahfouf and Rabier*, 2000]. Daily forcing fields were obtained from 24-hour forecasts started from operational analyzes at 12 Universal Coordinated Time (UTC) of each of the days for the years 2001 to 2005.

3. Model validation

In this section we will show that the model is able to reproduce main characteristics of the observed intraseasonal variability in the tropical Atlantic. First we will compare simulated and altimeter sea level anomalies (SLA, *http://www.jason.oceanobs.com*, SSALTO/DUACS gridded mean SLA). To focus on the intraseasonal time scales the time series are band-pass filtered (10-150 days). The spatial distributions of the stan-

dard deviation of the simulated and observed SLA are very similar (Fig. 1a and b). Both distributions show strongest fluctuations in the region of the NBC retroflection and the NECC with standard deviations of more than 5 cm and a weaker secondary maximum south of the equator ranging from 2-4 cm (Fig. 1a and b).

At the equator the SLA variations are generally weak but that does not mean that the intraseasonal variability of the circulation is weak here as well, which can be seen for instance in the eddy kinetic energy (EKE) of the model simulation. Note that EKE was calculated using velocity fluctuations relative to seasonal means to exclude the seasonal cycle. It contains, however, variability of time scales from days to years but is dominated by the intraseasonal time scales (not shown). Furthermore, the simulated SLA variability at the equator is larger compared to the observations. It is a well known feature of the altimeter derived SLA products to show less variance than eddy-resolving models, which is related to the resolution of the observations and their data processing [*Eden and Böning*, 2002; *Fratantoni*, 2001]. Compared to the observations, however, simulated variance is slightly larger compared to the observations at the mooring position (Figure 1). We note the caveat that this model/data disagreement might influence the comparison between the measurements and the model results.

In the model simulation DAILY (CLIM is similar, not shown however), the EKE in the western and central equatorial Atlantic is of comparable magnitude as in the North Brazil Current (NBC) retroflection/NECC region (Fig. 1c). Such strong velocity fluctuations at intraseasonal time-scales at the equator are consistent with moored current observations at 23°W [*Grodsky et al.*, 2005; *Brandt et al.*, 2006] and can be seen best in

the meridional velocity fluctuations (Fig. 2a). Meridional velocity on the equator shows intraseasonal fluctuations as the dominant signal, predominantly at time scales of about one month. These signals tend to show a maximum during boreal summer to boreal winter and often a minimum in spring. During maximal events, downward propagation of energy below the EUC is observed [*Brandt et al.*, 2006]. In addition, interannual changes in the strength of the intraseasonal fluctuations are found in the velocity data. The simulated meridional velocities on the equator at 23°W are as well dominated by intraseasonal fluctuations (Fig. 2b and c). The intraseasonal fluctuations intensify in June to March and reach down to more than 600m depth with clear indication of vertical energy propagation. Note that the intensity of the intraseasonal fluctuations differ from year to year in both simulations, in DAILY as well as in CLIM.

The observed meridional velocity fluctuations show two distinguishable signals between 20-40 days and at 14 days (Fig. 3a), from which the latter was found to have the characteristic of a Yanai wave [*Bunge et al.*, 2007], which is supposed to be excited by quasi-biweekly meridional winds in the eastern equatorial Atlantic [*Han et al.*, 2007]. The fluctuations of meridional velocity at periods related to TIWs (20-40 days) are intensified in the upper 120 m of the water column but reach down to 600m (Fig. 4).

A comparison of the mooring measurements with the model simulations DAILY and CLIM shows that simulated meridional velocity at 23°W peaks as well at 20-40 days periods, although more sharply bounded, with a pronounced near-surface intensification (Figure 3b and c). Fluctuations related to TIWs are narrow banded in the simulations and more energetic at depths. In addition, the peak of energy in the mooring measure-

ments moves from 20 days near the surface to 40 days at 600m depth (Figure 3a). In the simulations, energy is high from 20 to 40 days in the near surface layer and dominates at 600 m depth at about 40 days period. Toward higher frequencies, however, the power spectral density decreases more strongly in the simulations. The biweekly fluctuations that are low in the CLIM simulation are slightly enhanced in the DAILY simulation but still much weaker compared to the observations. The likely reason of this model bias is too low biweekly variability in the wind stress forcing, which is a known problem of atmospheric circulation models including the ECMWF model from which we took the forcing functions for DAILY (T. Jung, pers. comn.). However, we will not further discuss the biweekly signal since the focus of the present study is on the generation of intraseasonal variability by instability processes.

The season of strongest TIWs in the equatorial Atlantic starts in boreal summer, but events of wave propagation have also been observed in the first half of the year [e.g. *Weisberg and Weingartner*, 1988]. As already discussed above and by *Brandt et al.* [2006], monthly fluctuations in the meridional velocity measurements are dominated by these summertime events (Figures 2a and 4a). Fluctuations of about monthly period during boreal winter are present mostly in January to March. As expected from earlier studies, the fluctuations in late boreal summer are more pronounced compared to the signal in the first half of the year. In contrast to similar fluctuations in zonal velocity, the patterns are not confined to mixed layer depths [see also *Grodsky et al.*, 2005]. During the time of strong summer TIW events in 2005, high energy levels can be found in the upper 600 m associated with an indication of a downward energy propagation (Figure

4a). In the near surface layer, energy starts to grow in May 2005 and peaks between July to August. In September 2005 to February 2006, energy increases at 200-600m depth.

As already discussed above, there are strong differences in strength of the about monthly signal between individual years, e.g. energetic fluctuations in boreal summer 2005 and comparable little energy in summer 2004. This interannual modulation can be especially seen in the appearance of the winter signal. For instance, in boreal winter 2005, a distinctive pattern of the TIW signal exists, whereas in the first half of 2004 the signal is missing (Figure 4a).

The simulated meridional velocities at 23°W also show a seasonally modulated TIW signal with strong maxima in boreal summer (June to September) and incidental events from January to March (Figure 4b). Similar to the observations, the simulated TIW signal is surface intensified. Enhanced energy levels reach down to more than 600 m depth. Although slower compared to the observations, vertical energy propagation is evident in the model simulation.

The model results regarding the DAILY simulation show a distinct interannual modulation of the TIW signal. Energy levels become strongest in the second half of the years 2001 and 2004 and remain low in 2005. These simulated interannual variations differ from the observed ones. Both, the discrepancy between the observations and the DAILY simulation with realistic forcing and the fact that the CLIM simulation generates interannual variability (Figure 4c) suggests a largely non-deterministic behavior (stochastic variability) on interannual time scales, which contrast the more deterministic seasonal

modulation of TIWs. Although the generation of TIWs is seasonally modulated, the strength of the events appear stochastic. This conclusion is in general agreement with the model results of *Jochum and Murtugudde* [2004] indicating that a substantial part of the interannual variability in the tropical Pacific Ocean is generated by internal variability at the center of the TIW activity.

4. Oscillating patterns in the equatorial basin

A useful tool to extract oscillating patterns from multivariate time series is the evaluation of principal oscillating patterns [POPs hereafter *von Storch et al.*, 1988, 1995]. We will discuss here POPs of simulated unfiltered meridional velocities (v) taken from DAILY (exp. CLIM gave similar results, not shown however) at a zonal section along the equator and a meridional section along 23°W in order to shed light on the oscillating nature of the TIWs in space and time in different regions of the tropical Atlantic. Along the equator, about 16% of the total variance of v can be explained by an oscillating pattern with a period of ca 20-40 days (Figure 5a and b), i.e. can be directly related to the TIWs. The time-dependent amplitudes of the spatial patterns shown in Figure 5 are seasonally modulated and change from year to year. For example, the signal is strong in boreal winter 2001/2002, but less intense during other winters. Note that such interannual modulations are also evident in the wavelet analysis (Figure 4b).

The POP shown in Figure 5 describes an oscillation in space and time and can be explained as follows: During mid of August, for example, the amplitude of the imaginary part (Figure 5c) shows maximum values while the real part drops to zero (bold line in Figure 5a). This state of the POP thus corresponds to the imaginary spatial pattern of

the POP (Figure 5c). A region of positive meridional velocity is evident for example in the near surface layer directly east of 23°W. As time goes on, at the end of August the amplitude of the real POP pattern is at its maximum, while now the imaginary part is close to zero. This state of the POP corresponds thus to its real spatial pattern (Figure 5d). The pattern of northward velocity is shifted further west, i.e. close to 23°W, i.e. the whole pattern propagates with a phase velocity of about 0.3 ms^{-1} to the west. The oscillation is completed by the remaining sequence of the negative imaginary pattern and the negative real pattern of the POP with an overall period of ca. 30 days (Figure 5b). The signal of westward propagation is evident from the western boundary to about 0°E, where the signal appears to diminish.

The POP analysis of v along the 23°W section sheds light on the meridional distribution of the pattern related to the TIWs (Figures 6 and 7). The dominant POP picks up an oscillating fluctuation also at periods of 20-40 days and explains about 36% of total variance of meridional velocity along that section (Figure 6a and b). The signal is again seasonally modulated with maximum values predominantly in boreal summer. The dominant structure of the amplitude of the POP is given by a maximum north of the equator between about 2°-5°N in the upper 100 m with a secondary maximum at the equator (Figure 6c).

The second POP of the simulated meridional velocity along the 23°W section (Figure 7) explains about 14% of total variance with a period of ca. 20-40 days, i.e. can also be related to the TIWs. The imaginary and real amplitudes show maxima predominantly during January to March and July to September, but the seasonal modulation of the

signal is weaker than before. The spatial pattern of the second POP is maximum slightly south of the equator and is also strongest in the upper 100 m (Figure 7c).

5. Generating eddy kinetic energy in the tropical basin

In this section we will show that the intraseasonal fluctuations (TIWs) in the model simulation - showing up at different regions and with different seasonal modulation - have also different generation mechanisms. We consider the EKE $\bar{e} = \frac{\overline{u'^2+v'^2}}{2}$ where u' and v' represent deviations of the horizontal velocity from seasonal means, denoted by $\bar{u}$ and $\bar{v}$, which are averaged over 6 years of experiment CLIM (results from DAILY are similar). Note that we use the EKE as a measure for intraseasonal variability, i.e. for the kinetic energy contained in the TIWs. The budget for EKE is given by

$$\bar{e}_t + \nabla \cdot (\bar{\mathrm{u}}\bar{e} + \mathrm{M}) \;=\; \bar{S} + \overline{b'w'} - \epsilon \qquad (1)$$

where $\bar{S} = -\overline{\mathrm{u}'u'} \cdot \nabla\bar{u} - \overline{\mathrm{u}'v'} \cdot \nabla\bar{v}$ represents energy transfer from the seasonal mean kinetic energy (MKE) to EKE due to horizontal shear instability. Note that $\bar{S}$ is also sometimes called energy production rate due to barotropic instability. Negative $\bar{S}$ indicates transfer to EKE. The energy production term $\overline{b'w'}$ in Eq. (1), where b denotes buoyancy and w vertical velocity, describes energy transfer from eddy potential energy (EPE) to EKE and is sometimes called EKE production due to baroclinic instability. Negative $\overline{b'w'}$ indicates transfer to EKE. Dissipation of EKE by unspecified small-scale processes is denoted by ϵ and remaining advective components in Eq. (1) are collected in the vector $\mathrm{M} = \overline{\mathrm{u}'e} + \overline{\mathrm{u}'p'}$, where p' denotes pressure fluctuations. Note that in a basin-wide integral, the advective terms on the left hand side of Eq. (1) will cancel at

the boundaries so that the integrated energy production rates $\bar{S}$ and $\overline{b'w'}$ will balance dissipation and temporal changes. Since the advective terms thus only redistribute the EKE we will show the production rates $\bar{S}$ and $\overline{b'w'}$ only. Since the TIWs are strongly seasonally modulated, energy transfer terms are shown for the different seasons.

Figure 8 shows $\bar{S}$ in the tropical Atlantic averaged over the upper 50 m depth. The upper 50m depth are chosen since areas of horizontal and vertical shears are strongest at these depths. The barotropic instability production rate, $\bar{S}$, is large in the northern hemisphere, in particular near the western boundary, while south of the equator much smaller magnitudes of $\bar{S}$ show up. Within the NECC and in a region just north of the equator, large negative values of $\bar{S}$ are extending into the interior of the tropical Atlantic. Note that approaching the western boundary, $\bar{S}$ tends to change sign. In this region the advective terms in Eq. 1 (not shown) play a more dominant role than in the interior of the ocean, and no clear picture can be derived from the EKE budget.

Within the NECC region, the seasonal cycle of EKE is large and EKE is generated by barotropic instability predominantly in the second half of the year. In the region just north of the equator, negative values of $\bar{S}$ show up throughout the year. Here, the intensity also varies with the seasons and the influence of $\bar{S}$ becomes strongest in the second half of the year. Just south and along the equator, $\bar{S}$ is positive indicating that the fluctuations are feeding energy back into the mean currents. In an averaged sense, however, the EKE production (negative $\bar{S}$) dominates the transfer from EKE to Mean Kinetic Energy (MKE) (positive $\bar{S}$) in all seasons.

Figure 9 shows seasonal maps of $\overline{b'w'}$, also averaged over the upper 50 m. At the equator, $\overline{b'w'}$ is almost vanishing in all seasons, while a few degrees latitude off the equator $\overline{b'w'}$ becomes as large as the energy production due to horizontal shear of the mean currents. In fact, the baroclinic production term $\overline{b'w'}$ is large in both hemispheres, in contrast to the energy production rate $\bar{S}$. Close to the western boundary and within the NECC, the sign of $\overline{b'w'}$ fluctuates hampering for $\bar{S}$ a clear interpretation of the generation mechanism. However, in the central tropical Atlantic, predominantly negative values of $\overline{b'w'}$ appear between the equator and 5° latitude on both sides of the equator which are strongest in July to September and more or less vanish in January to March.

Figure 10 shows zonally averaged (30°W to 10°W) energy production rates $\bar{S}$ and $\overline{b'w'}$ together with the mean zonal currents. It is clear that the production terms can be related to the horizontal and vertical shear of the mean zonal flow. The EKE near the equator is generated by horizontal shear instability between the eastward EUC and the westward nSEC. This signal shows up all year long, although stronger in the second half of the year. The horizontal shear between the westward nSEC and the eastward flowing NECC is related to the large values of $\bar{S}$ at about 4°-5°N predominantly occurring during boreal summer and persists till boreal winter. This seasonal modulation is consistent with the strength of the NECC, which is strongest in boreal summer, while in spring, near surface flow within the NECC is comparably sluggish or even westward [*Richardson and Reverdin*, 1987] and $\bar{S}$ is almost vanishing. In the northern hemisphere, the energy production by $\bar{S}$ is supported off the equator by energy production due to baroclinic instability, which is related to the vertical shear of the nSEC. In contrast, for the TIW

signal in the southern hemisphere horizontal shear production plays no role, it is entirely driven by the vertical shear of the cSEC.

6. Conclusion

The analysis of the spatial and temporal distribution of TIWs in the Atlantic Ocean using a combination of current observations at the equator at 23°W and a realistic eddy-resolving 1/12° general circulation model of the Atlantic Ocean shows that the energy for the waves is drawn from the mean flow via horizontal and vertical shear instability at three different locations. In the central tropical Atlantic, EKE is high between 4°-5°N, along the equator and between 4°-5°S (Figure 1c). The off-equatorial areas of EKE production are characterized by a remarkable seasonal modulation [*Jochum and Malanotte-Rizzoli*, 2003]. An analysis of the EKE budget in the model simulation revealed that especially within the NECC, the seasonal cycle of EKE is generated by horizontal shear instability ($\bar{S}$) predominantly in the second half of the year. This seasonal modulation is consistent with the strength of the NECC, which is strongest in late boreal summer, while in spring the near surface flow within the NECC region is comparable sluggish or even reversed and $\bar{S}$ is almost vanishing. The seasonal maps of the EKE production terms further show that other regions of maxima in EKE in the tropical Atlantic are fed by different sources in the EKE budget: In the northern hemisphere, barotropic and baroclinic instabilities contribute to the generation of EKE. Along the equator, barotropic instabilities prevail while in the southern hemisphere, only baroclinic instability accounts for the production of EKE.

The comparison of the zonally averaged (30°W to 10°W) production rates of EKE and the mean zonal currents reveals that the instability processes can be related to the horizontal and vertical shears of the mean zonal flow (Figure 10). In the northern hemisphere, EKE is generated by baroclinic instability in the vertical shear of the nSEC and by barotropic instability in the horizontal shear between the nSEC and the NECC. Along the equator, EKE is produced in the area of the horizontal shear between the EUC and the nSEC and production rates reach down to about 100 m depth. South of the equator, baroclinic instability was identified as the only source of EKE related to the vertical shear of the cSEC. The baroclinic instability in the southern hemisphere is slightly weaker than in the northern hemisphere due to the smaller SST gradient in the southern hemisphere.

The observations and the model show that TIWs are intensified in the upper 100 m of the water column, and that the signal reaches down to 600 m depth. As already reported by *Brandt et al.* [2006] by using a subset of the mooring data presented here, we find indications of a downward energy propagation from the near surface layer down to 600 m depth, which is present during the time of strong summer TIW events in both, the observations and the model simulations. However, lateral and vertical dispersion of EKE away from the region where it isparticular generated appears to be different in the simulations compared to what can be observed. This is in particular evident in the spectral distribution of meridional velocities (Figure 2) as well as in the different observed and simulated vertical energy propagation (Figure 4). Possible reasons for this could be the low bias in strength of the intraseasonal (biweekly) variability in the wind

forcing (T. Jung, pers. comn.), as well as the missing atmospheric feedback on TIWs which appears to reduce the growth of TIWs [*Seo et al.*, 2007].

A POP analysis reveals that along the equator, westward propagating oscillations with phase velocities of about 0.3 ms^{-1} exist from the western boundary to about 0°E. The signal is intensified slightly during January to March and July to September (Figures 5 and 7). North of the equator, oscillations related to TIWs between 4°-5°N are characterized by a strong seasonal modulation (Figure 6). Although the oscillations are at a similar period range, this difference in the seasonal modulation already indicates that TIWs along and north of the equator do not share the same generating mechanisms. Different to the Pacific Ocean where two types of TIWs coexist at the same time with distinct periods [*Lyman et al.*, 2007], different types of TIWs coexist as well in the Atlantic Ocean but at a similar period range [*Bunge et al.*, 2007]. Using the model simulations it could be figured out that three areas of TIW generation coexist in the central tropical Atlantic. The identification of different types of TIWs is a question that remains to be explored.

Both the observations and model results show a strong interannual modulation of the TIW signal. However, the years of strong TIW events in the observations differ from those simulated by the model driven by realistic forcing (DAILY simulation). The chaotic and unpredictably nature of the hydrodynamic instabilities generating the TIWs might be an explanation for the inconsistency of the interannual changes in the intensity of the TIW signal. We also found an increase in TIW intensity when forcing the model with daily wind stress compared to a model experiment using monthly mean wind stress

forcing. Note that both the temporal (daily vs. monthly) and the spatial (40 km vs. approx. 200 km) resolution of the wind stress forcing were enhanced. However, reasons for interannual fluctuations of TIWs and the dependency of their intensity on small scale wind stress forcing needs to be addressed in future research.

Acknowledgements:

Workhorse ADCP data are provided via the TAO project office at NOAA/PMEL in collaboration with many research institutes listed on the PIRATA web site *http://www.pmel.noaa.gov/pirata/*. This work was supported by the Deutsche Bundesministerium für Bildung und Forschung (BMBF) as part of the Verbundvorhaben Nordatlantik under contract 03F0443B. The authors also thank Thomas Jung for providing the high resolution ECMWF surface forcing time series. The model integrations have been performed at the computing center at the University Kiel, Germany and at the Deutsches Klimarechenzentrum (DKRZ), Hamburg, Germany.

Notes

1. The numerical code together with all configurations used in this study can be accessed at *http://www.ifm-geomar.de/∼spflame*.

References

Barnier, B., L. Siefridt, and P. Marchesiello (1995), Thermal forcing for a global ocean circulation model using a three year climatology of ECMWF analysis, *J. Marine Sys.*, *6*, 363–380.

Brandt, P., F. Schott, C. Provost, A. Kartavtseff, V. Hormann, B. Bourlès, and J. Fischer (2006), Circulation in the central equatorial Atlantic: Mean and intraseasonal to

seasonal variability, *Geophys. Res. Lett.*, *33*, doi:10.1029/2005GL025498.

Brandt, P., V. Hormann, B. Bourlès, J. Fischer, F. Schott, L. Stramma, and M. Dengler (2007), Oxygen tongues and zonal currents in the equatorial Atlantic, *J. Geophys. Res.*, accepted.

Bunge, L., C. Provost, and A. Kartavtseff (2007), Variability in horizontal current velocities in the central and eastern equatorial Atlantic in 2002, *J. Geophys. Res.*, *112*, doi:10.1029/2006JC003704.

Eden, C., and C. Böning (2002), Sources of Eddy Kinetic Energy in the Labrador Sea, *J. Phys. Oceanogr.*, *12*, 3346–3363.

Eden, C., R. Greatbatch, and J. Willebrandt (2007), A diagnosis of thickness fluxes in an eddy-resolving model, *J. Phys. Oceanogr.*, *37*, 727–742.

Fratantoni, D. (2001), North Atlantic surface circulation during the 1990's observed with satellite-tracked drifters, *J. Geophys. Res.*, *106*, 22,067–22,093.

Grodsky, S., J. Carton, C. Provost, J. Servain, J. Lorenzzetti, and M. McPhaden (2005), Tropical instability waves at 0°N, 23°W in the Atlantic: A case study using Pilot Research Moored Array in the Tropical Atlantic (PIRATA) mooring data, *J. Geophys. Res.*, *110*, doi:10.1029/2005JC002,941.

Han, W., P. Webster, J.-L. Lin, W. Liu, R. Fu, and D. Yuan (2007), Dynamics of intraseasonal sea level and thermocline variability in the equatorial Atlantic during 2002-2003, *J. Phys. Oceanogr.*, in press.

Haney, R. (1971), Surface thermal boundary condition for ocean circulation models, *J. Phys. Oceanogr.*, *1*, 79–93.

Jochum, M., and P. Malanotte-Rizzoli (2003), On the generation of North Brazil Current rings, *J. Marine Res.*, *61*, 147–173.

Jochum, M., and R. Murtugudde (2004), Internal variability of the tropical Pacific Ocean, *Geophys. Res. Lett.*, *31*, doi:10.1029/2004GL020488.

Jochum, M., P. Malanotte-Rizzoli, and A. Busalacchi (2004), Tropical instability waves in the Atlantic Ocean, *Ocean Modelling*, *7*, 145–163.

Kelly, B., S. Meyers, and J. O'Brien (1995), On a generating mechanism for Yanai waves and the 25-day oscillation, *J. Geophys. Res.*, *100*, 10,589–10,612.

Lyman, J., G. Johnson, and W. Kessler (2007), Distinct 17- and 33- day tropical instability waves in subsurface observations, *J. Phys. Oceanogr.*, *37*, 855–872.

Mahfouf, J.-F., and F. Rabier (2000), The ECMWF operational implementation of four-dimensional variational assimilation. II: Experimental results with improved physics, *Quar. J. Roy. Meteor. Soc.*, *126*, 1171–1190.

McCreary, J., and Z. Yu (1992), Equatorial dynamics in a 2 1/2-layer model, *Prog. Oceanogr.*, *29*, 61–132.

Pacanowski, R. (1995), MOM 2 documentation, User's guide and reference manual, Technical Report, GFDL Ocean Group.

Peter, A., M. L. Hénaff, Y. du Penhoat, C. Menkes, F. Marin, J. Vialard, G. Caniuax, and A. Lazar (2006), A model study of the seasonal mixed layer in the equatorial Atlantic, *J. Geophys. Res.*, *11*, doi:10,1029/2005JC003157.

Philander, S., W. Hurlin, and R. Pacanowski (1986), Properties of Long Equatorial Waves in Models of the Seasonal Cycle in the Tropical Atlantic and Pacific Oceans,

J. Geophys. Res., *91*, 14,207–14,211.

Rabier, F., H. Järvinen, E. Klinker, J.-F. Mahfouf, and A. Simmons (2000), The ECMWF operational implementation of four-dimensional variational assimilation. I: Experimental results with simplified physics, *Quar. J. Roy. Meteor. Soc.*, *126*, 1143–1170.

Richardson, P., and G. Reverdin (1987), Seasonal Cycle of Velocity in the Atlantic North Equatorial Countercurrent as Measured by Surface Drifters, Current Meters, and Ship Drifts, *J. Geophys. Res.*, *92*, 3691–3708.

Seo, H., M. Jochum, R. Murtugudde, A. Miller, and J. Roads (2007), Feedback of Tropical Instability-Wave-Induced Atmospheric Variability onto the Ocean, *J. CLim.*, *20*, 5842–5855.

Stevens, D. (1990), On open boundary conditions for three dimensional primitive equation ocean circulation models, *Geophys. Astrophys. Fluid Dynamics*, *51*, 103–133.

von Storch, H., T. Bruns, I. Fischer-Bruns, and K. Hasselmann (1988), Principal oscillation pattern analysis of the 30- to 60-day oscillation in general circulation model equatorial troposphere, *J. Geophys. Res.*, *93*, 11,022–11,036.

von Storch, H., G. Bürger, R. Schnur, and J. von Storch (1995), Principal Oscillation Patterns: A Review, *J. CLim.*, *8*, 377–400.

Weisberg, R., and T. Weingartner (1988), Instability waves in the equatorial Atlantic ocean, *J. Phys. Oceanogr.*, *18*, 1641–1657.

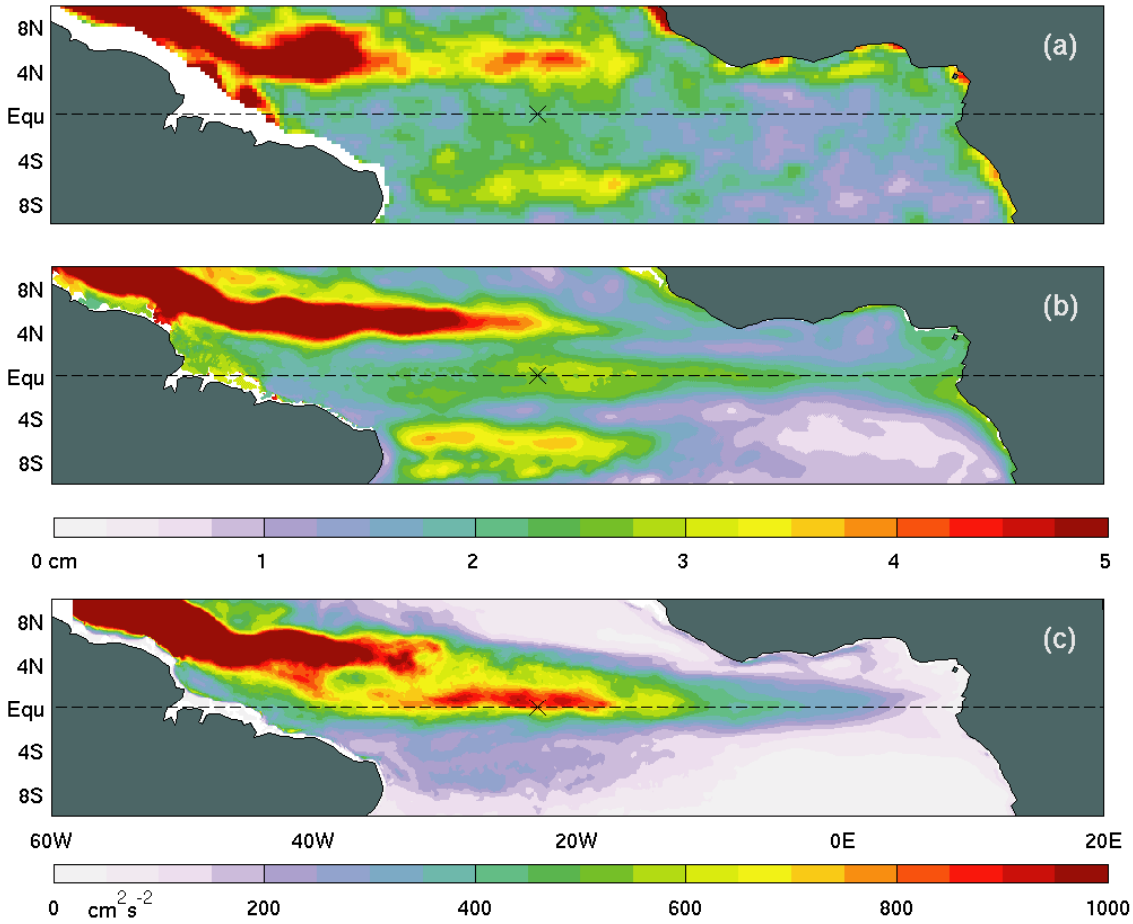

Figure 1. *Standard deviations of sea level anomalies during July to September 2001-2004 derived from (a) SSALTO/DUACS altimeter measurements (http://www.jason.oceanobs.com) and (b) the DAILY simulation. (c) Eddy kinetic energy (EKE) evaluated from the DAILY simulation during July to September 2001-2004. Each time series is band-pass filtered 10-150 d in time. The mooring position at 23° W at the equator is marked.*

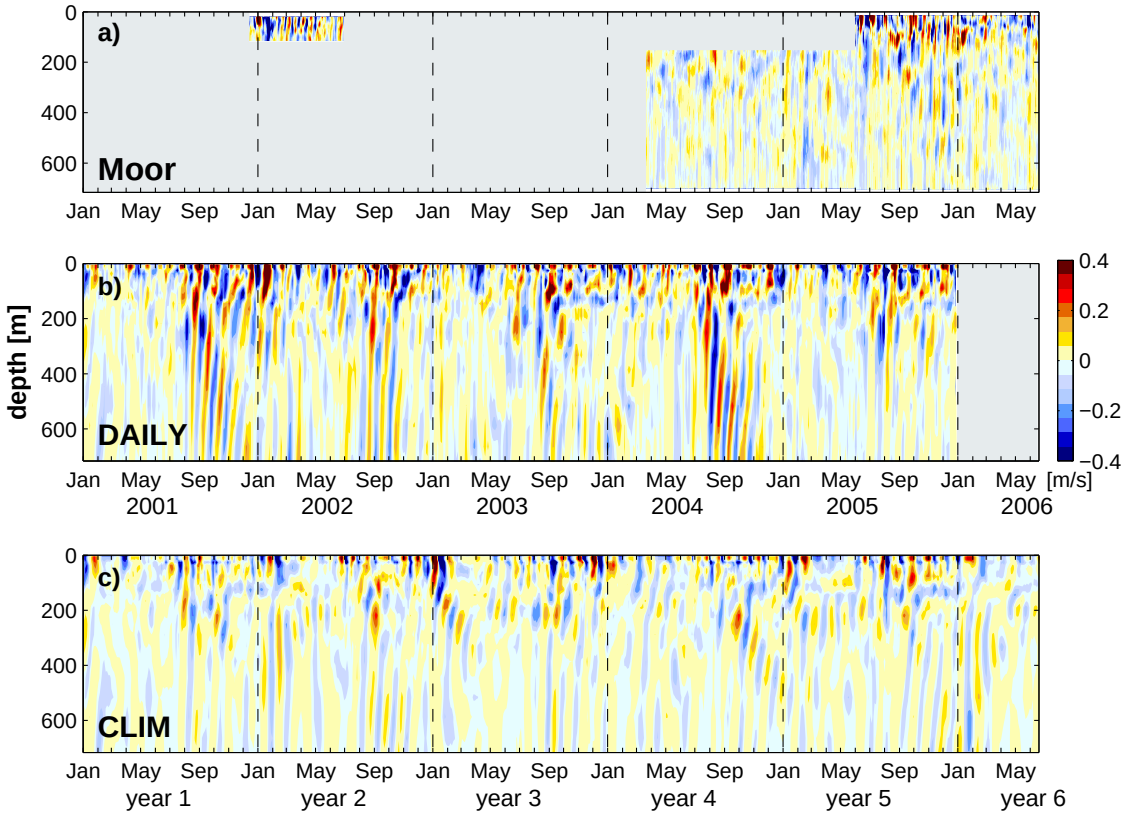

Figure 2. *Meridional velocity at 23° W at the equator from (a) 300kHz WH-ADCP and 75kHz LongRanger ADCP, (b) he DAILY simulation (2001-2005) and (c) the CLIM simulation (six years). Data are detided, small data gaps were interpolated. Dashed line marks the beginning of each year. Gaps in (a) are due to missing measurements (light gray shaded).*

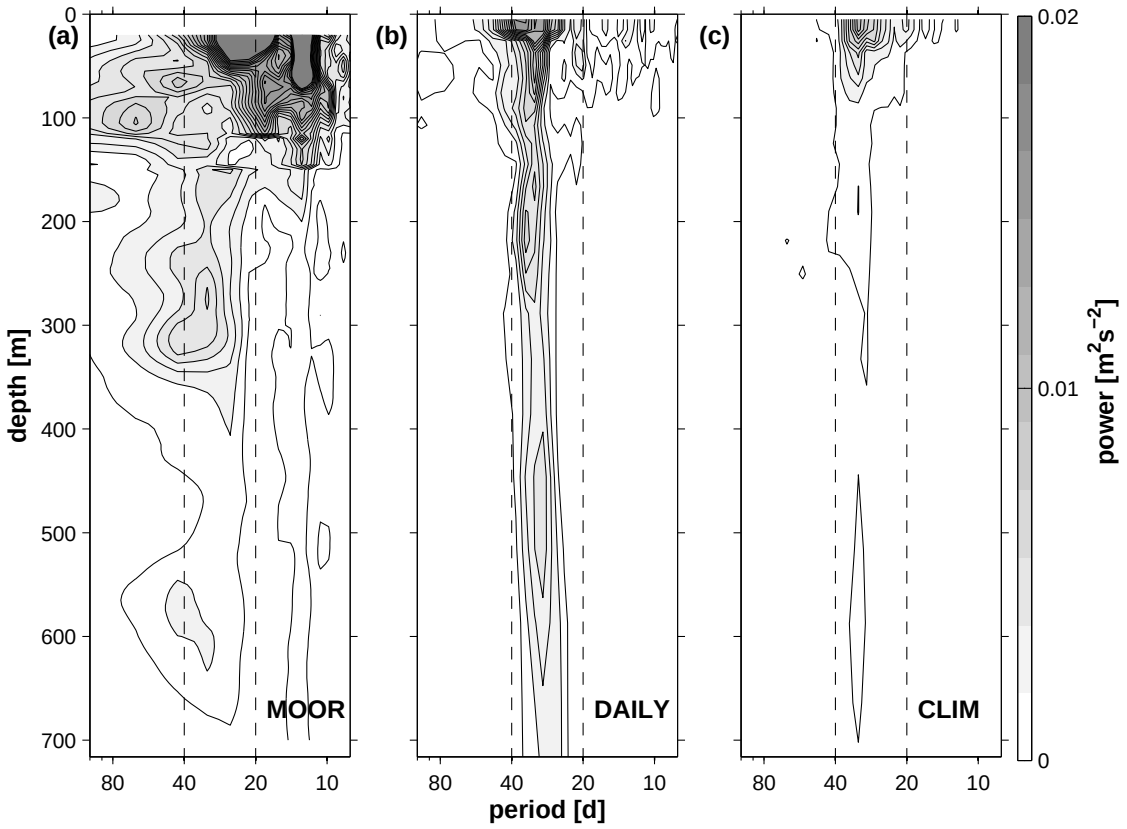

Figure 3. *Vertical distribution of variance conserved power spectral density of meridional velocity at the equator using (a) mooring array measurements (2002-2006), (b) the DAILY simulation (2001-2005) and (c) the CLIM simulation (six years) at 23° W at the equator. Solid line box marks the period range of 20 to 40 days.*

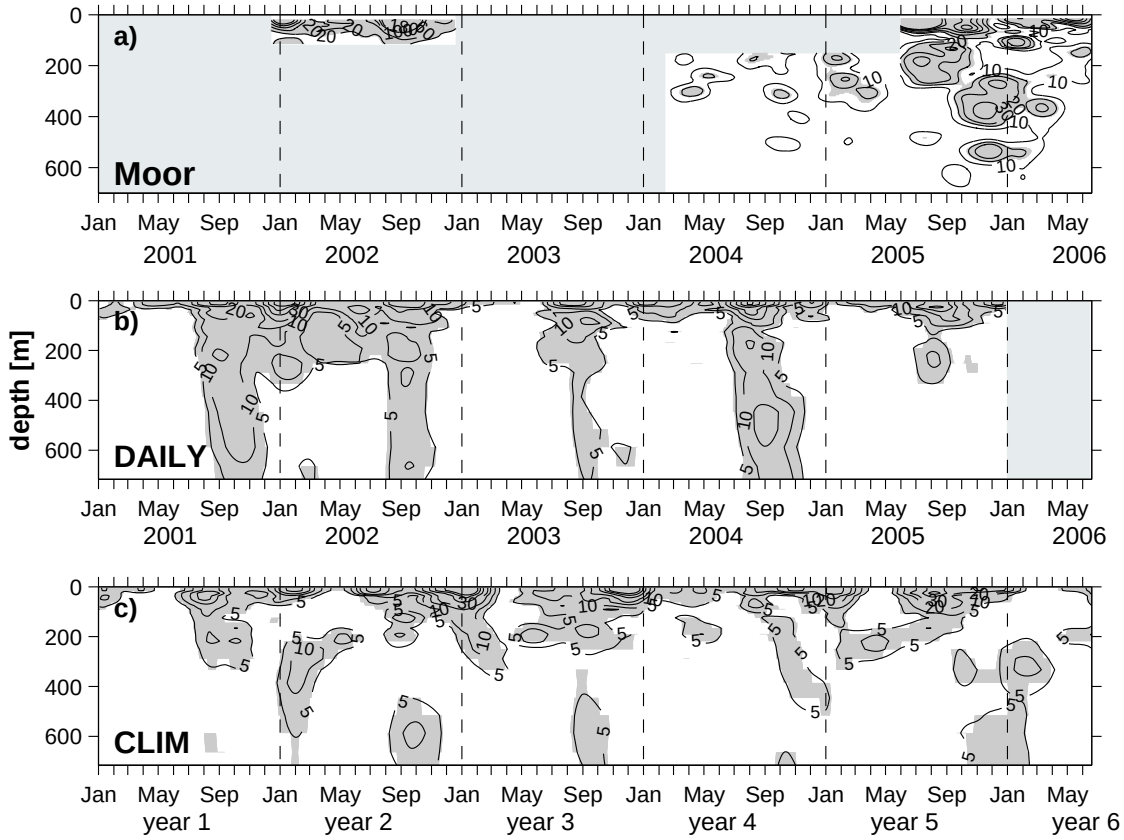

Figure 4. *Normalized wavelet energy distributed with depths, averaged over a period range of 20 to 40 days derived from (a) current measurements, (b) the DAILY simulation and (c) the CLIM simulation at 23° W at the equator. Gaps in (a) are due to missing measurements (light gray shaded). Values above the 95% significance level are shaded dark gray and the black dashed line indicates the beginning of each year.*

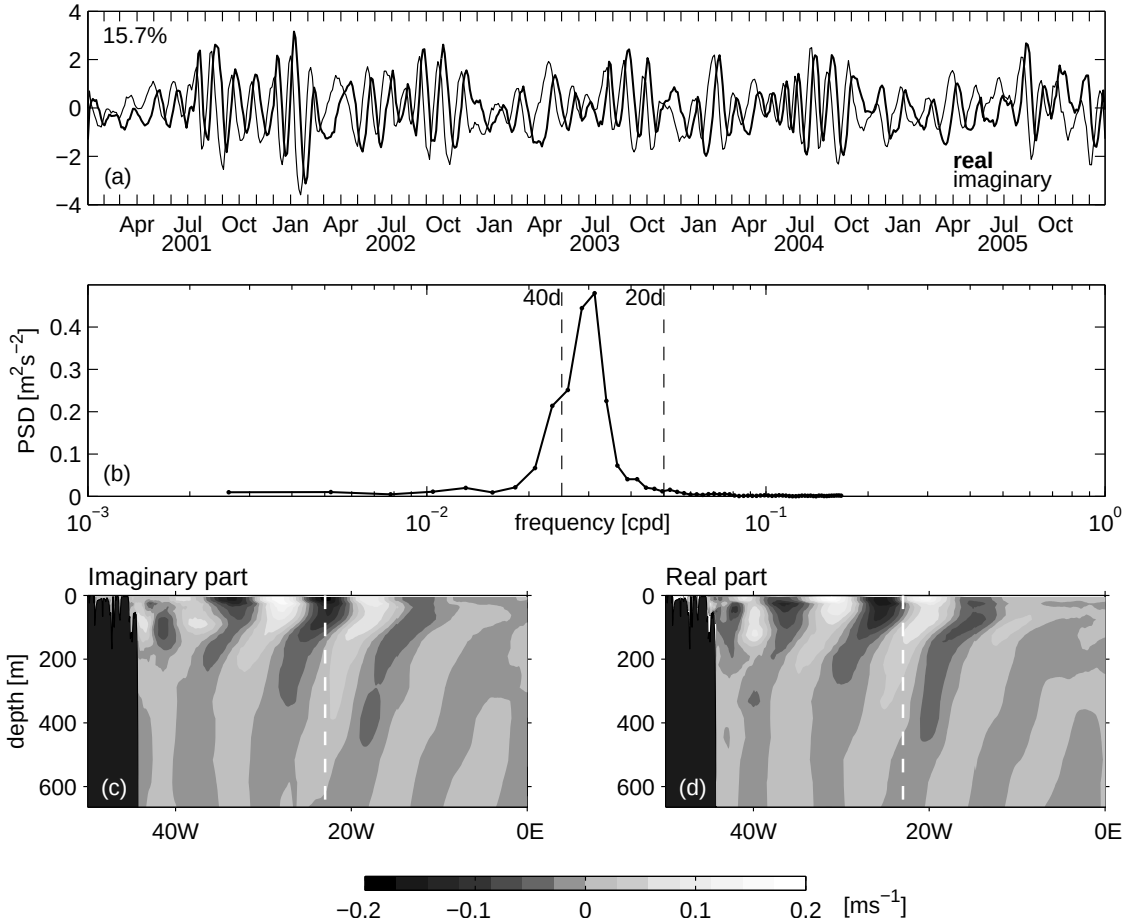

Figure 5. *Principal Oscillating Pattern (POP) analysis using DAILY simulated meridional velocity along the equator. (a) real (bold line) and imaginary part of the non-dimensional coefficients of the first POP and (b) corresponding power spectral density. (c) imaginary and (d) real part of the dominant POP pattern. The 23° W longitude is marked with a dashed white line.*

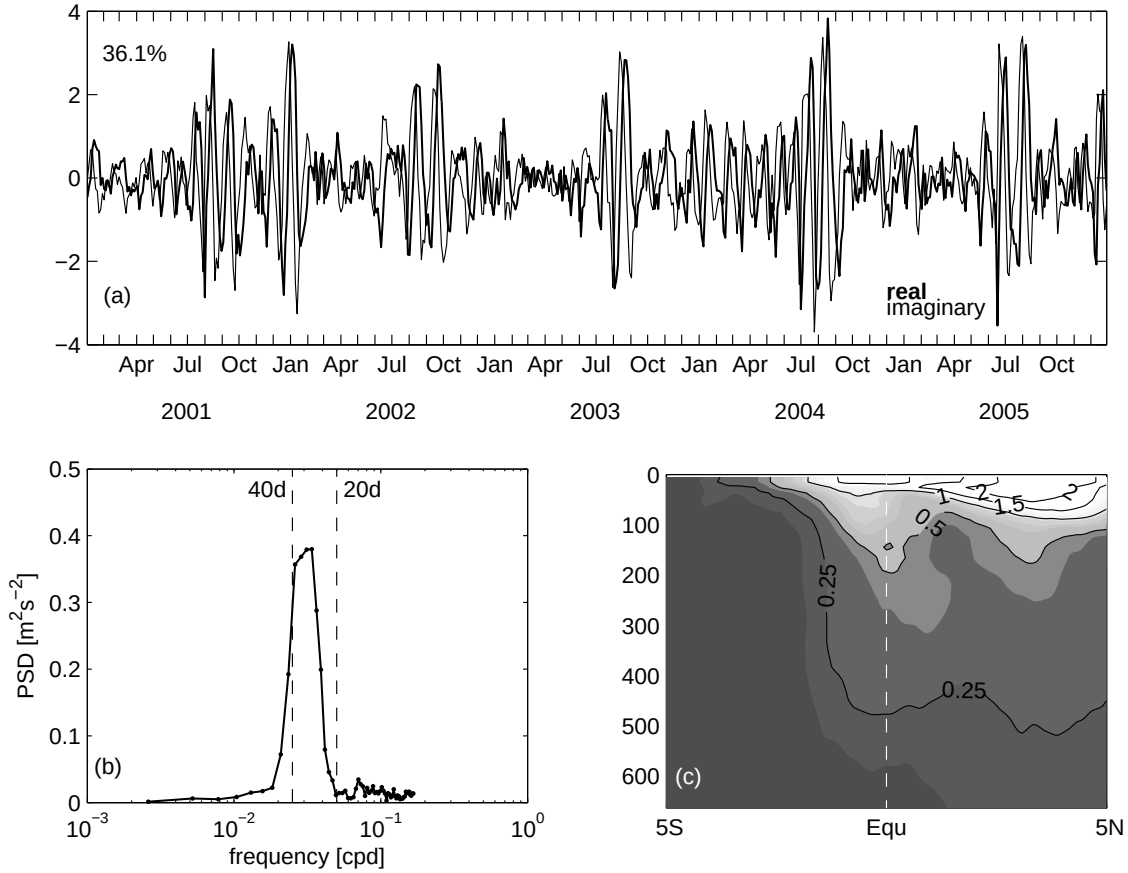

Figure 6. *POP analysis using DAILY simulated meridional velocity along the 23° W section. (a) real (bold) and imaginary part of the non-dimensional coefficients of the first POP and (b) corresponding power spectral density.(c) amplitude of the dominant POP, contours are in cms^{-1}. The equator is marked with a dashed white line.*

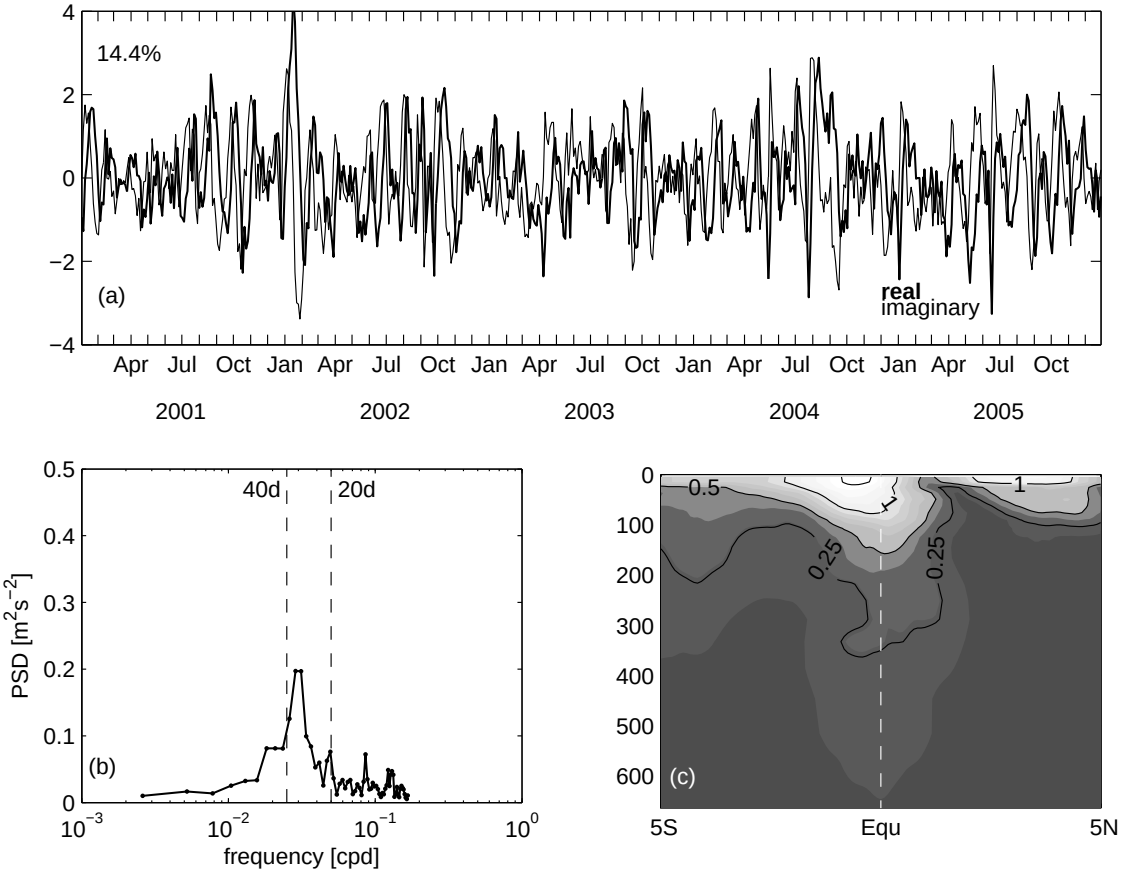

Figure 7. *Same as Figure 6, but for the second POP.*

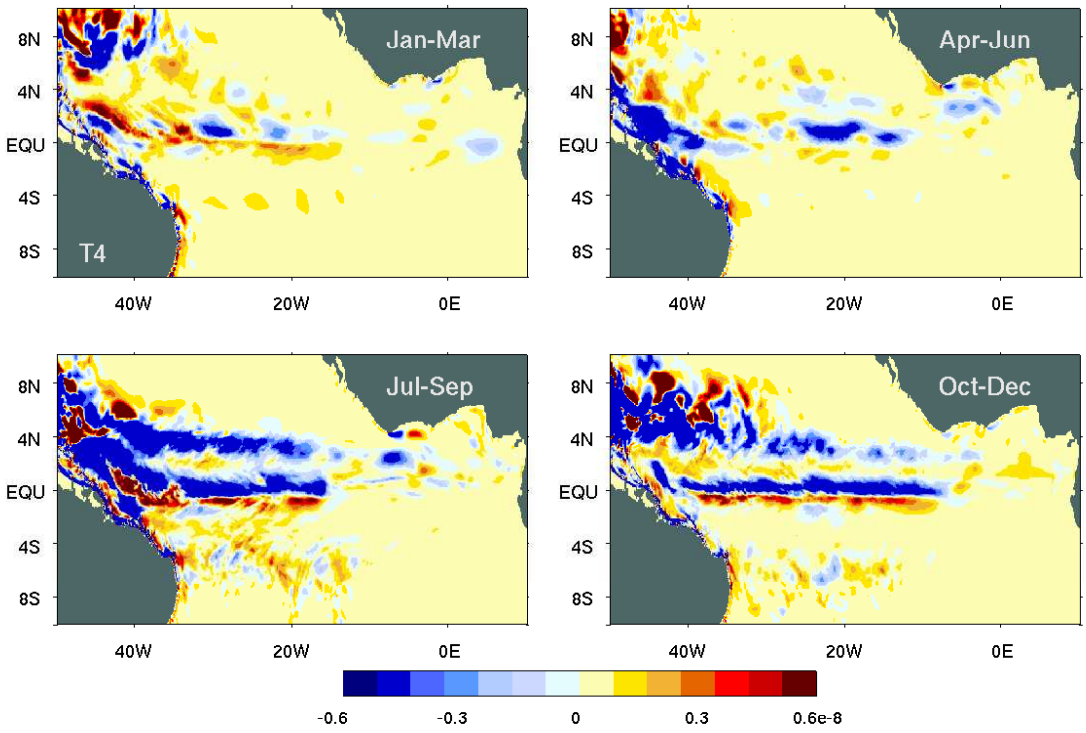

Figure 8. *Seasonal maps of the barotropic instability production rate $\bar{S}$ ($[m^2 s^{-3}]$, equation 1), derived from six years of the CLIM model simulation and averaged over the top 50 m. Negative sign denotes transfer into the fluctuation.*

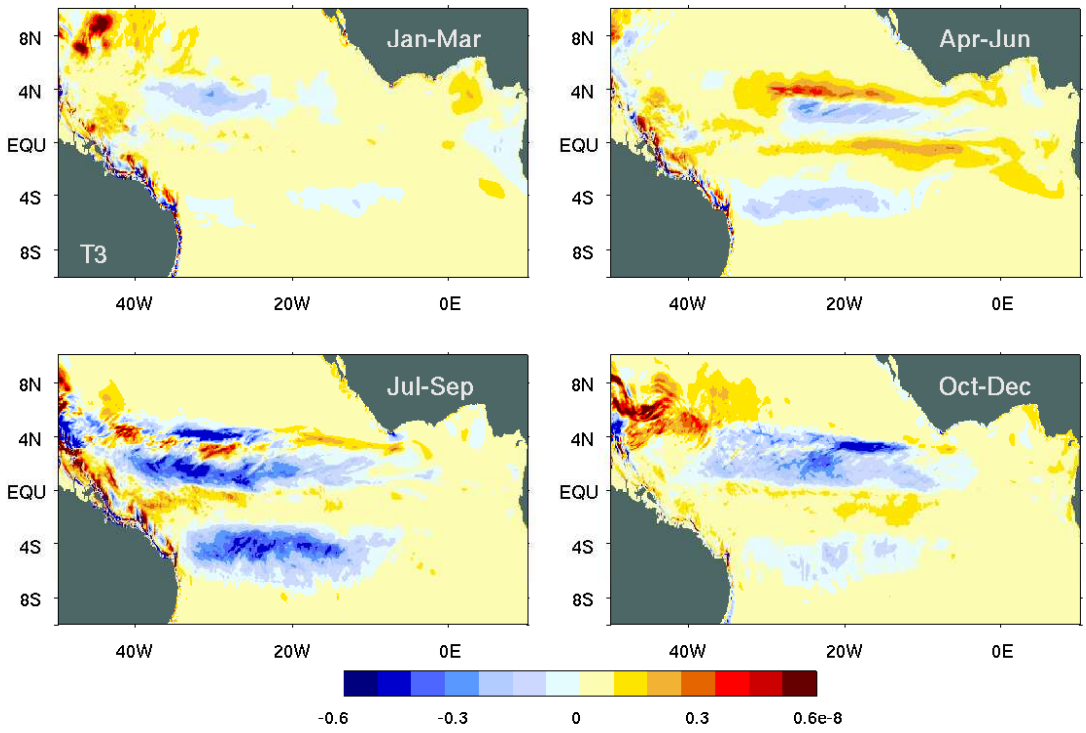

Figure 9. *Seasonal maps of the baroclinic production term $\overline{b'w'}$ ($[m^2 s^{-3}]$, equation 1), derived from six years of the CLIM model simulation and averaged over the top 50 m. Negative sign denotes transfer from EPE into EKE.*

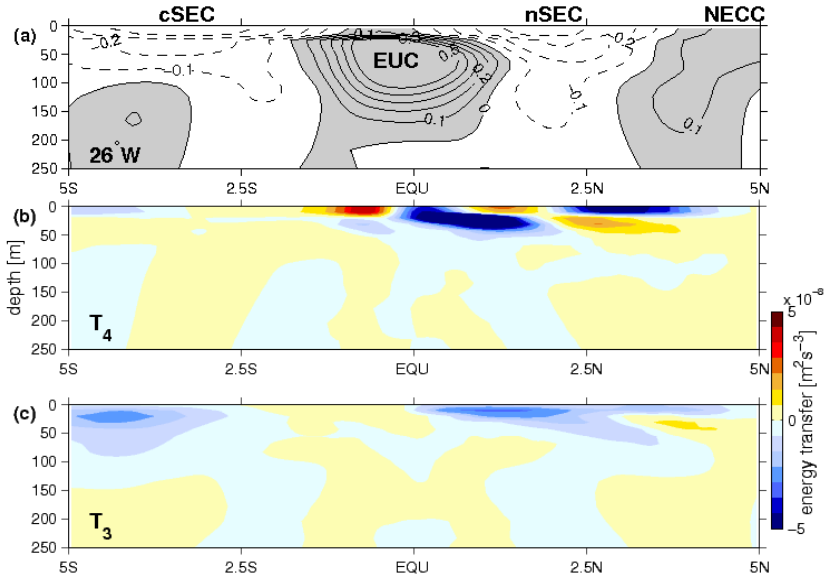

Figure 10. *Results from six years of the CLIM simulation. a) Mean zonal velocity along 26° W, showing the central and northern South Equatorial Currents (cSEC and nSEC), the Equatorial Under Current (EUC) and the North Equatorial Counter Current (NECC). (b) Barotropic production rate $\bar{S}$ averaged from 30° W to 10° W. Negative sign denotes transfer into EKE. (c) Corresponding average of the baroclinic production term $\overline{b'w'}$. Negative signs denote transfer into EKE.*